Fatigue and biological properties of Ti-6Al-4V ELI cellular structures with variously arranged cubic cells made by selective laser melting

M. Dallago[a,*], V. Fontanari[a], E. Torresani[a], M. Leoni[b], C. Pederzolli[c], C. Potrich[c,d], M. Benedetti[a]

a Department of Industrial Engineering, University of Trento, Trento, Italy

b Department of Civil, Environmental and Mechanical Engineering, University of Trento, Trento, Italy

c Laboratory of Biomolecular Sequence and Structure Analysis for Health, Fondazione Bruno Kessler, Trento, Italy

d Institute of Biophysics, CNR, Trento, Italy

*Contacting Author:
Michele Dallago
Tel. +390461282457
Fax +390461281977
E-mail: michele.dallago@unitn.it

ABSTRACT

Traditional implants made of bulk titanium are much stiffer than human bone and this mismatch can induce stress shielding. Although more complex to produce and with less predictable properties compared to bulk implants, implants with a highly porous structure can be produced to match the bone stiffness and at the same time favor bone ingrowth and regeneration. This paper presents the results of the mechanical and dimensional characterization of different regular cubic open-cell cellular structures produced by Selective Laser Melting (SLM) of Ti6Al4V alloy, all with the same nominal elastic modulus of 3GPa that matches that of human trabecular bone. The main objective of this research was to determine which structure has the best fatigue resistance through fully reversed fatigue tests on cellular specimens. The quality of the manufacturing process and the discrepancy

between the actual measured cell parameters and the nominal CAD values were assessed through an extensive metrological analysis. The results of the metrological assessment allowed us to discuss the effect of manufacturing defects (porosity, surface roughness and geometrical inaccuracies) on the mechanical properties. Half of the specimens was subjected to a stress relief thermal treatment while the other half to Hot Isostatic Pressing (HIP), and we compared the effect of the treatments on porosity and on the mechanical properties. The fatigue strength seems to be highly dependent upon the surface irregularities and notches introduced during the manufacturing process. In fully reversed fatigue tests, the high performances of stretching dominated structures compared to bending dominated structures are not found. In fact, with thicker struts, such structures proved to be more resistant, even if bending actions were present.

Keywords: additive manufacturing, biocompatibility, cellular materials, defects, fatigue

1. INTRODUCTION

Nowadays, metals are the best choice for load-bearing biomedical implants. Ceramics present high corrosion resistance and enhanced biocompatibility, but in general are too brittle and have low fatigue resistance, while polymers have inadequate mechanical properties for this application (Ryan, 2006; Singh, 2010; Wu, 2014). Among metals, titanium alloys are employed in applications where high performance is requested, e.g. the aerospace and biomedical fields. In the fabrication of biomedical implants, Ti alloys are in general preferred to other metals such as stainless steel and Co-alloys because of their high resistance-to-weight and stiffness-to-weight ratios and good corrosion resistance (Li, 2014; Long, 1998; Murr, 2010). In addition, they are biocompatible (Long, 1998; Rack, 2006; Niinomi, 2008), most likely thanks to the thin oxide layer that forms very rapidly on the metal surface (Singh, 2016).

Traditional implants made of solid Ti present some crucial drawbacks that push researchers to find new kinds of implant materials. In fact, solid titanium, with an elastic modulus of 110 GPa, is much stiffer than human bone, which has an elastic modulus varying from 20 GPa of cortical (outer) bone to 2 GPa of trabecular (internal) bone (Zhao, Li, Hou, Hao, Yang, Murr, 2016). This stiffness mismatch causes the implant to take most of the load thus leaving the bone under-loaded: this is known as stress shielding. The living bone tissue adapts to the lower stresses and thus bone resorption will occur, leaving behind a weaker structure that could cause the implant to loosen (Ahn, 2017; Dabrowski, 2010; Tan, 2017). Moreover, solid implants show low anchorage over time (Albrektsson, 2010; Tan, 2017) because of the weak bone tissue attachment and regeneration

ha eliminato:

ha eliminato: appears

ha eliminato: load bearing

(Dabrowski, 2010). To get implants that match the elastic modulus of the bone and at the same time favor bone ingrowth and regeneration, a good solution is to build them with a porous structure (Dabrowski, 2010; Tan, 2017). A graded lattice structure of the implant allows for a further reduction of bone resorption (Khanoki, 2013). A pore size between 490 and 1100 μm has been observed to produce high bone stabilization, although the best performance is shown by pores of 600 μm (Taniguchi, 2016). The interconnectivity of the pores has been proved to be crucial in promoting tissue infiltration and the necessary nutrient flow (Otsuki, 2006; Ryan, 2006; Tan, 2017; Taniguchi, 2016).

Additive manufacturing (AM) is the most promising manufacturing technique for porous metallic implants as it allows the pore size, the pore size distribution and the pore morphology to be precisely controlled (Taniguchi, 2016; Zhao, Li, Hou, Hao, Yang, Murr, 2016). Moreover, through AM complicated shapes and customized implants can be easily produced (Tan 2017). The two most widely used AM techniques for titanium and its alloys are Selective Laser Melting (SLM) and Electron Beam Melting (EBM). Both techniques consist in melting a micrometric metal powder in overlapping layers to build up a solid structure, the key difference being the heat source used to melt the particles: the former uses a laser beam, the latter an electron beam (Campoli, 2013; Tan, 2017; Zhao, Li, Zhang, 2016). SLM has a greater precision than EBM due to a smaller spot size of the laser, but is slower (Tan, 2017). The as-built microstructure obtained via SLM is characterized by prior β grains and within those grains martensitic α' platelets dominate. On the other hand, the EBM as-built microstructure consists generally of prior columnar β grains and within those grains an α+β phase can be found because of the slower cooling compared to the SLM process. Thus, the SLM microstructure (martensitic) has higher yield strength, but lower ductility compared to the EBM microstructure (Gong, 2015; Murr, 2012; Tan, 2017; Vrancken, 2012; Zhao, Li, Zhang, 2016).

Despite the considerable advantages of AM, metallic artifacts produced with this technology can be affected by various defects, namely residual stresses, porosity, surface roughness and geometrical irregularities. Detrimental residual stresses can be reduced with post-manufacturing thermal treatments, which also improve the ductility of the microstructure (although at the cost of small reduction in strength). Residual stresses affect especially artifacts produced via SLM. One of the most popular treatments applied to Ti alloys produced by AM is Hot Isostatic Pressing (HIP), which consists in simultaneously applying hydrostatic pressure and high temperature to the component by submerging it in a fluid. HIPing has multiple effects: it modifies the microstructure by coarsening the grains and by decomposing α' martensite into α lamellae and it reduces internal porosity (Benedetti, 2017; Leuders, 2013; Qiu 2013; Tammas-Williams, 2016; Van Hooreweder, 2017;

ha eliminato: have

Wauthle, 2015; Zhao, Li, Zhang, 2016). Porosity is mainly caused by the entrapment of gases (spherical pores) and incomplete melting of the powder particles (irregular pores) (Gong, 2015; Tammas-Williams, 2016; Zhao, Li, Zhang, 2016). Some pores can be also carried over from the precursor powder (Qiu 2013). HIPing is effective in reducing porosity (Leuders, 2013), although spherical pores are more difficult to close via HIPing compared to irregular ones (Qiu, 2013). Pores in SLM products are generally irregular, while in EBM products pores are more spherical (Zhao, Li, Zhang, 2016). Geometrical defects are present as non-uniform strut thickness along its length and strut waviness (Zargarian, 2016). Unmelted and partly melted powder particles in the proximity of the melt can become attached to the surface, greatly increasing the surface irregularity (Zhao, Li, Zhang, 2016). It is interesting to add, thou, that geometrical irregularities (non-uniform strut thickness, missing struts) are not a-priori negative for structures to be employed in biomedical applications, as observed by Luxner (Luxner, 2007; Luxner, Stampfl, 2009; Luxner, Woesz, 2009b). Irregularities decrease the strength and the stiffness of the structure, but they also make it less sensitive to localized deformations and in general more robust to load direction variation.

The α+β Ti6Al4V is the most popular Ti alloy for biomedical load-bearing implants because of a good combination of strength and ductility (Rack, 2006), despite the potential toxicity of V has drawn attention to the need to develop new alloys with enhanced biocompatibility (Long, 1998; Zhao, Li, Hou, Hao, Yang, Murr, 2016). The mechanical properties (quasi-static and fatigue) of Ti6Al4V cellular structures produced via AM for a given unit cell depend both on the microstructure and the amount and type of defects. The yield stress and the ductility mainly depend on the microstructure and have a very weak dependence upon residual porosity (Gong, 2015; Qiu, 2013; Zhao, Li, Hou, Hao, Yang, Murr, 2016; Zhao, Li, Zhang, 2016). On the other hand, Ti-alloys in general have high notch sensitivity (Long, 1998; Niinomi, 2008), so fatigue resistance is strongly influenced by defects that act as stress raisers (Leuders, 2013; Gong, 2015). This is an important issue, given that fatigue resistance is a critical aspect when load-bearing biomedical implants are considered (Zhao, Li, Hou, Hao, Yang, Murr, 2016). However, there are few studies on the fatigue behavior of AM Ti6Al4V cellular structures and all describing only compression-compression fatigue tests (Hrabe, 2011; Li, 2012; Yavari, 2013; Yavari, 2015; Zhao, Li, Hou, Hao, Yang R., Misra, 2016; de Krijger, 2017). From these tests, it results that structures made of unit cells characterized by prevalently axial actions in the struts are more resistant to fatigue (Yavari, 2015; Zhao, 2016). Moreover, if the fatigue resistance of the structures is normalized by their yield stress, structures with the same unit cell but different porosities behave the same; that is, for same values of porosity, different unit cells behave differently (Yavari, 2013; Yavari, 2015). In practice, this means that once the curve of the normalized fatigue strength as a function of the number of cycles

ha eliminato: has been

ha eliminato:

ha eliminato:

for a unit cell type is known, the S-N curve for any other structure of the same unit cell type (with different porosity and/or strut thickness) can be calculated by multiplying the normalized curve by the yield stress of the structure considered. This observation brings to the conclusion that cellular materials, although structures on the small scale, behave as materials when their homogenized macroscopic properties are considered (Yavari, 2013). The effect of the stress ratio *R* on fatigue strength was investigated by de Krijger et al. (2016) and they observed that loading under high *R*-ratios resulted in greater number of cycles to failure. They observed a strong influence of the load amplitude, while the effect of the mean stress was weak. The presence of notches and geometrical irregularities appears to be the most likely explanation, given that in bulk Ti notches reduce the fatigue strength but also the sensitivity to the mean stress. Van Hooreweder et al. (Van Hooreweder, 2017) investigated possible treatments to improve the fatigue resistance of SLM Ti6Al4V cellular structures. They concluded that HIPing and stress relief thermal treatments are positive as they increase the ductility of the as-built microstructure (ductile α+β phase). The effect of the reduction of pores internal to the struts due to HIPing is very small on fatigue resistance. HIPing followed by chemical etching has proven to be the most effective treatment because it also removed surface stress raisers.

Commentato [MB1]: Immagino ti riferisca a test compression-compression. Forse è meglio specificarlo

This paper presents the results of the fully reversed fatigue tests and metrological characterization of different regular open-cell cellular structures produced by SLM of Ti6Al4V alloy. The aim is to contribute towards the understanding of the fatigue behavior of cellular structures by carrying out fully reversed fatigue tests, which, to our best knowledge, have never been done before. Six different configurations of the cubic unit cell were chosen: in three the cubes are simply shifted to fill the 3D space, while in the other three the cubic cells are skewed to obtain structures with a cylindrical symmetry. These structures are intended to be employed in the production of fully porous orthopedic implants.

The quality of the manufacturing process and the discrepancy between the actual measured cell parameters and the nominal CAD values were assessed through an extensive metrological analysis. The results of the metrological assessment allowed us to gain some understanding on the effect of manufacturing defects (porosity, surface roughness and geometrical inaccuracies) on the mechanical properties. The fracture surfaces of the cell walls of the specimens broken by fatigue were observed by SEM and the fracture behavior of each structure is discussed based on these observations. The effect of HIPing on porosity and on the mechanical properties was investigated by applying this treatment to half of the specimens.

2. MATERIALS AND METHODS

In the following section, we will describe the design procedure of the specimens used in the experimental investigation carried out in the frame of this research. Then some considerations on the manufacturing procedure will be presented and finally the experimental procedures will be described.

2.1 Specimen design

Six different open-cell cellular structures were considered in this work (Figure 1): regular cubic cells (CUB NS), single staggered cubic cells (CUB S), double staggered cubic cells (CUB 2S), regular cylindrical cells (CYL NS), single staggered cylindrical cells (CYL S) and double staggered cylindrical cells (CYL 2S). The main goal of this work was to identify the structure with the highest fatigue resistance through fully reversed fatigue tests. All the structures were designed with care in eliminating every sharp notch. The sections of the cell walls are thus circular, and all the junctions are filleted with the same nominal radius. The elastic has been measured and compared with the values calculated via the FE method applied to the CAD models. The manufacturing quality of the specimens have been assessed by comparing the nominal dimensions of the unit cell (form the CAD models) with the measured values.

The structures with cylindrical symmetry were developed with the idea of perfectly filling a cylindrical volume with cubic cells without the necessity to cut unit cells while keeping low the boundary effects. It can be interesting from the biological point of view that the cylindrical arrangement leaves a channel centered on the axis of the structure that should considerably enhance the transport properties parallel to the same axis.

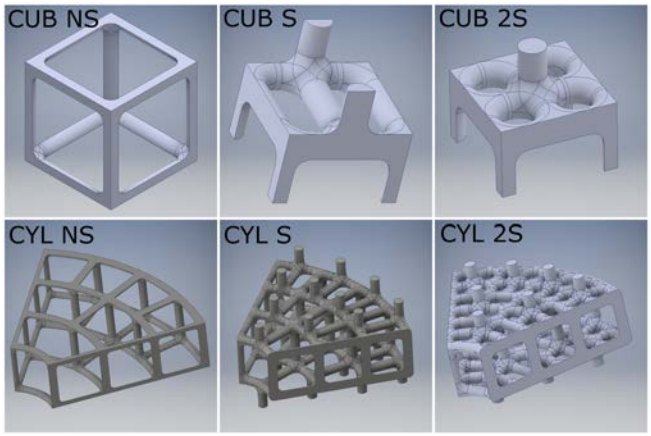

Figure 1. CAD models of the unit cells of the six cellular structures studied in this work.

The geometrical parameters that characterize each cell are the cell wall length L, the cell wall thickness t_0 (the section of the cell walls is a circle, thus t_0 is in fact a diameter) and the fillet radius R.

The simplest specimens (CUB NS and CUB S) were designed according to a procedure developed previously by the authors for 2D cellular structures (Dallago, 2017) and extended to the 3D case as illustrated in the following paragraph. The others were designed via a trial-and-error procedure based on the FE method. The design procedure consists in a simple optimization procedure according to which the unit cell parameters (cell wall length, cell wall thickness and junction fillet radius) are chosen based on the requirements listed in Table 1.

Table 1. Requirements for the unit cell parameters.

Quantity	Target value	Notes
Elastic modulus (E_{yy})	3 GPa	Trabecular bone stiffness
Cell wall length (L)	1.500 mm	Ensure large pores for improved osseo-integration
Cell wall diameter (t_0)	$\geq$ 0.200 mm	Should be the smallest possible (limited by 3D printer accuracy)
Fillet radius (R)	$\approx t_0/2$	(limited by 3D printer accuracy)

The cellular structures represented by the specimens are intended to be used in the production of fully porous orthopedic implants, thus the main requirement is to match the elastic modulus of trabecular bone to avoid the stress shielding effect, as discussed in the Introduction. The stiffness target value was thus set to 3 GPa, which is a reasonable estimate of the elastic modulus of human trabecular bone. To ensure proper osseo-integration, i.e. to permit the adherence and reproduction of osteoblasts on the structure of the implant and the proper flow of nutrients until full bonding is achieved, sufficiently large pores must be present. The pore size target is of at least 400-800 μm to ensure maximum osseo-integration. After a benchmark analysis of the 3D printers available on the market, the smallest cell wall diameter allowed was set to 200 μm because this is the smallest achievable detail size. Given these considerations the cell wall length was fixed to 1500 μm. The fillet radius between the cell wall junctions was imposed to be equal to the half of the cell wall diameter as a simplification.

There are some reasons behind the fact that such structures have been chosen. The cubic structures are in general the simplest to conceive, design and produce. The regular one has a very high stiffness to weight ratio because it is stretching dominated, while the other two are more compliant (given the same relative density) because they are bending dominated. Bending dominated structures present some advantages regarding their use in implants if we consider the failure process. In fact, although weaker (with respect to stretching dominated structures of the same density), under compression these structures fail more gradually, avoiding sharp decreases in loading capacity when buckling occurs and thus matching the behavior of the highly irregular structure of the human bone (Luxner, Woesz, 2009).

Design procedure

The design procedure of the specimens involves the following steps, in order:

1. Estimation of the unit cell parameters t_0 and R based on the conditions summarized in Table 1. This was done via analytical equations or FE modeling depending on the structure. This will be further discussed in the following paragraphs.
2. Convergence analysis on the number of unit cells that should be included in the specimen to reduce border effects.
3. Buckling analysis to verify that the structures don't fail by instability at the loads applied in the fatigue tests.
4. Design of the part connecting the thread to the cellular part of the specimen. This was done according to the UNI-5710 norm

The CUB-R structure could be designed to meet the required stiffness by adapting the semi-analytical model developed in (Dallago, 2017) for 2D structures to the 3D case. The elastic modulus calculated for the 2D regular cubic cell (RR) structure can be used to obtain the stiffness of the corresponding 3D regular square cell structure with cell walls of square section simply by multiplying the 2D stiffness E2D by the cell wall thickness t_0 normalized by the cell wall length L:

$$E^*_{3D}\big|_{SQ} = E^*_{2D}\big|_{SQ}\,\frac{t_0}{L} \tag{1}$$

The real 3D structure has a circular section of diameter t_0, thus it is clearly less stiff than the corresponding structure with square sections of side t_0. On the other hand, if we correct the previous

equation to take into account this fact, the elastic modulus can be obtained with the following formula:

$$E^*_{3D}\big|_{CIRC} = E^*_{2D}\big|_{SQ}\,\frac{t_0}{L}\,\frac{\pi}{4} \tag{2}$$

This last relationship is expected to underestimate the elastic modulus of the 3D structure because the stiffening effect of the fillet radii in the third dimension is neglected. It appears reasonable to assume as the actual value the mean of the two previous expressions:

$$E^*_{3D} = \frac{E^*_{3D}\big|_{SQ} + E^*_{3D}\big|_{CIRC}}{2} \tag{3}$$

This consideration appears to be correct, as shown in Figure 2, where the stiffness of the regular square structure calculated from a parametric FE model based on the unit cell of Figure 1 is compared with the values obtained from the above expressions. Thus, we have obtained a reliable tool to predict the stiffness of 3D regular square cell structures considering also the fillet radius at the cell wall junctions.

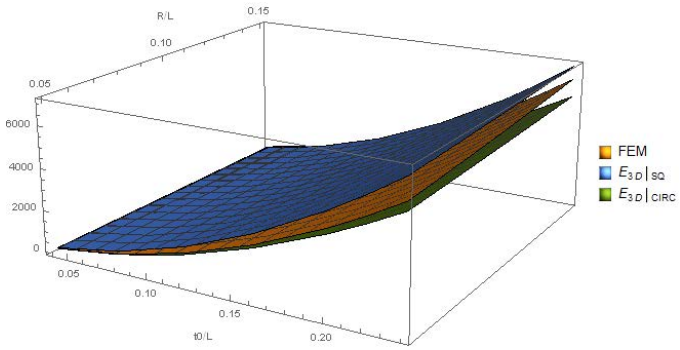

Figure 2. Surface plot of the stiffness of the unit cell as a function of the unit cell geometrical parameters. Comparison of the FE results and the estimates of Eqs. (1) and (2).

Substituting the values of the parameters of Table 1 into Eq. (3) directly gives the values of t_0 and R which represent a regular square cell structure of stiffness compatible with human bone. The same exact theoretical procedure can be applied also to the CUB-S structure to obtain the stiffness of the 3D structure from the 2D model developed in (Dallago, 2017).

Such a simple design procedure cannot be applied to the other structures because no corresponding analytical expressions for the stiffness are available. Thus, the only way is to solve via the FE method the unit cells of those structures to calculate the geometrical parameters that confer the target stiffness. This procedure is more complicated as it is essentially based on a trial and error approach until the criteria of Table 1 are met.

Apart from the elastic modulus, the other important requirement for these structures is fatigue resistance. To estimate it, the theoretical stress concentration factors have been calculated at the cell wall junctions via the FE method from the unit cell model. The maximum Stress Concentration Factor (SCF) for each cell has been considered; in fact, it is notable that particularly in the cylindrical structures not all the junctions are loaded in the same way and this will be discussed further in the next Section. The SCF is computed according to the following formula:

$$K_t = \frac{\bar{\sigma}_{\max}}{\sigma_n} \tag{4}$$

Where $\bar{\sigma}_{\max}$ is the maximum von Mises equivalent stress in the structure (occurring at one of the filleted junctions) and σ_n is the nominal homogeneous stress calculated by dividing the force applied to the cellular structure by its nominal cross section (i.e. the section measured as if the cellular material was a bulk material).

The size of the pores of each unit cell was calculated from the CAD model as the diameter of the largest sphere than can pass through neighboring cells (Arabnejad, 2016); in other words, is the smallest "hole" in the 3D lattice. This definition of pore size defines the interconnectivity of the cellular structure, which is a very significant parameter from the biological point of view. To avoid confusion with the internal porosity of the struts (which is due to the manufacturing process), we will refer to the lattice porosity as "unit cell pore size".

The values for the unit cell parameters and the corresponding elastic modulus and stress concentration factor for the six structures are reported in Table 2.

Table 2. CAD geometrical parameters of the cellular structures, effective elastic modulus and stress concentration factors (from FE applied to the CAD models).

Structure	t_0 (mm)	R (mm)	FE elastic modulus (MPa)	Minimum SCF	Maximum SCF	Relative density (%)	Unit cell pore size

							(mm)
CUB NS	0.260	0.130	3021	62	62	6.61	1.340
CUB S	0.340	0.170	3220	49	49	15.32	0.820
CUB 2S	0.350	0.175	3208	37	37	19.61	0.800
CYL NS	0.230	0.115	3000	54	58	6.04	
CYL S	0.300	0.150	2960	52	59	12.39	
CYL 2S	0.350	0.175	2480	49	68	18.39	

Staggering the unit cells permits to increase the cell wall thickness by preserving the same stiffness and thus to reduce the stress concentration factor. The behavior of the cylindrical structures is more complicated because the load is not uniformly distributed on the section and the value of the stress concentration factor at the junctions varies. Interestingly, the maximum intensity of the local peaks of stress increases by staggering the structure, but the minimum value decreases. This clearly indicates the non-uniform distribution of the force lines.

ha eliminato: keeping

ha eliminato: low

Specimen description

Each specimen is made up of a cylindrical cellular part connected to two threads, as shown in Figure 3. The threads are M10x1.5, as required by the testing machine.

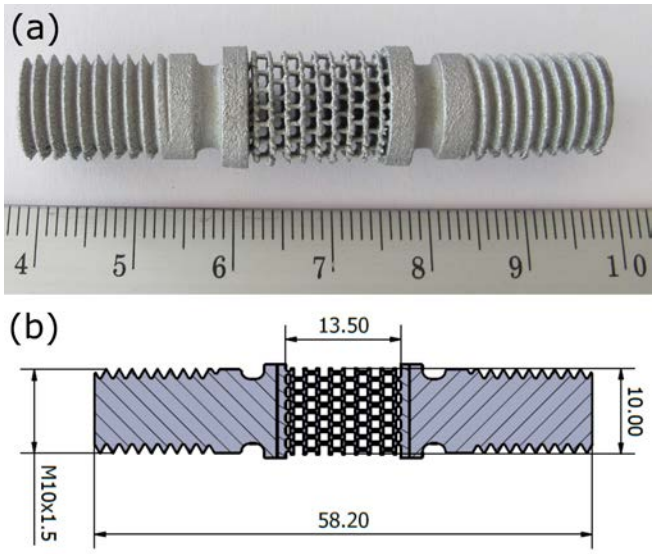

Figure 3. Example of specimen with the threaded heads for push-pull fatigue tests: (a) printed Ti alloy specimen; (b) longitudinal section of the CAD model (annotations in *mm*) The diameter of the cellular part is 10 mm for the cubic structures and 12 mm for the cylindrical ones.

A critical aspect is the connection of the cellular part to the base of the thread, which obviously is much stiffer. To avoid the failure of the specimen at that section, the cell walls have been made slightly thicker and are joined to the heads with a wide fillet. In addition, a relief groove has been added at the base of the thread according to the UNI EN 5710 norm to smooth off the flow of lines of force from the heads to the central cellular part.

The cellular part, regardless whether it has a cubic or a cylindrical symmetry, is cut in a circular shape, i.e. the nominal section of the specimen is a circle. The nominal diameter of the cellular part of the cubic structures is 10 mm while for the cylindrical structures is 12 mm. The height of the cellular part is 13.5 mm.

The number of unit cells that make up the specimen was chosen as the smallest possible that keeps border effects from substantially influencing the stiffness. Convergence analyses on the number of unit cells performed via the FE method indicate that the stiffness of the specimen matches reasonably well that of the unit cell when the size of the cellular specimen is 8 times L in height and 6 times L in width.

2.2 Specimen manufacturing

The fine details of the designed structures requested the use of a very fine powder. The specimens were additively manufactured via Selective Laser Melting (SLM) starting from biomedical grade Ti6Al4V ELI (Grade 23) in form of powder of mean diameter of 8.64 μm, shown in Figure 4. A distribution analysis of the powder was carried out (Figure 5).

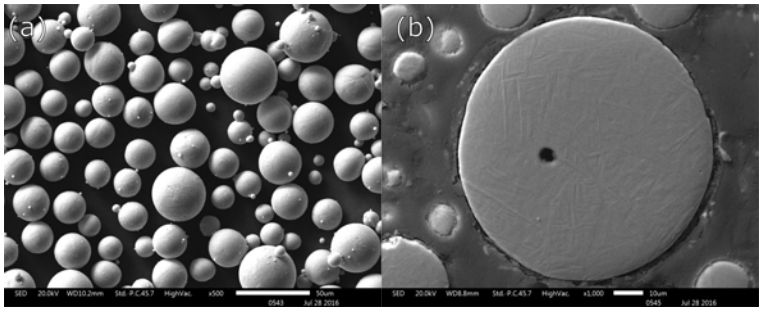

Figure 4. Ti6Al4V ELI powder use to produce the SLM cellular specimens. (a) Size distribution; (b) detail of a single particle.

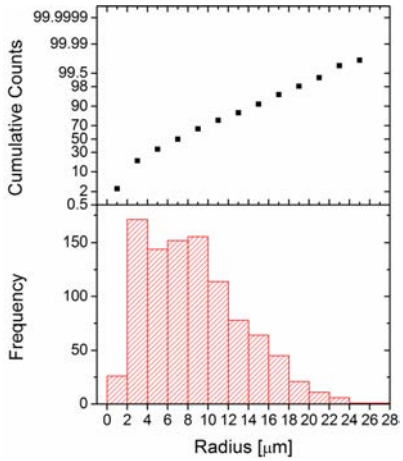

Mean	8.64 μm
Median	8.04 μm
St Dev	4.79 μm
Max	26.43 μm
Min	1.77 μm

Figure 5. Results of the size distribution analysis of the Ti6Al4V powder.

The specimens were built along a direction inclined by 45° with respect to the longitudinal one using a 3D System ProX DMP 300 printer. Further details are provided in (Benedetti, 2017).

The specimens were divided into two batches. The first was heat treated at 670° C for 5 hours in Ar protective atmosphere to relieve residual stresses (referred to as “as built”), the second was treated by Hot Isostatic Pressing (HIP) at 920° C and 1000 bar for 2 hours (referred to as “HIPed”) after sand blasting to remove the unmelted particles from the surface to prevent the HIP thermo-mechanical treatment from incorporating oxidized particles into the bulk, thus resulting in pores and lack-of-fusion defects.

2.3 Experimental analysis

The morphological, microstructural and mechanical properties were measured to have a complete characterization of the specimens (both as-built and HIPed). In this Section, the experimental procedures that were used will be briefly described.

Morphological and metallurgical characterization

The morphological properties of the cellular structures that were studied are the surface characteristics, the internal porosity of the struts, the actual cell dimensional parameters (t_0, R, L) to be compared with the design values from the CAD models and the microstructure.

To measure the porosity and the dimensional parameters, two sections were cut from each specimen as shown in Figure 6: a transversal and a longitudinal with respect to the loading direction. The sectioned samples are then mounted, ground using SiC abrasive papers (with 120, 180, 320, 400, 600, 1000, 1500 grit sizes), and polished using a 3-micron diamond paste and a 0.04-micron alumina suspension. A Kroll's etching is applied to reveal the microstructures.

Porosity is measured on three metallographic samples using image analysis software ImageJ® by counting the pores and calculating the area of each pore. Two different approaches were used to characterize the porosity of the specimens. The first and simplest method is to measure the sum of the area of the pores and express porosity as a percentage of the total area of the sectioned cell walls (area occupied by the cell walls):

$$\text{Porosity}\,[\%] = \frac{\sum \text{Area of pores}}{\text{Total area of section}} \times 100 \qquad (5)$$

The second is a statistical approach based on the statistics of extreme values and it allows to estimate the maximum pore size in the whole specimen based on the distribution of pore sizes on the analyzed section. This approach permits to estimate the maximum defect size to estimate the fatigue strength of a component [Beretta, 1998; Murakami, 2002]. The authors followed the procedure described in (Murakami, 2002), but here some aspects of the procedure are discussed for clarification:

ha eliminato: allows

- Two specimens (one as-built and one HIPed) for each structure were sectioned and mirror polished and the observable pores were counted and the area for each of them was measured.

- The square root of the projected area of each pore on the section $\sqrt{area}$ was calculated. It is useful to clarify that we did not choose a control area S_0 to look for the maximum defect (as instructed in (Murakami, 2002)), but we calculated S_0 a-posteriori by dividing the area of the section by the number of the pores counted. S_0 is necessary to calculate the return period T defined as $T = S/S_0$, where S represents the area of prediction, which is the total area of the section our case. T in thus the number of the counted pores.
- The expected maximum pore size on the section $\sqrt{area}_{\max}$ was estimated using the least squares method.
- As suggested in (Murakami, 2002), the data with cumulative probability $F < 10\%$ and $F > 85\%$ was excluded if deviating from linearity when performing the linear regression.

The estimation of fatigue life is based only on the size of the defects projected on the section normal to the loading direction. In this work, this statistical approach was applied only to estimate the largest pore in each structure. The estimation of the fatigue strength is left for future work.

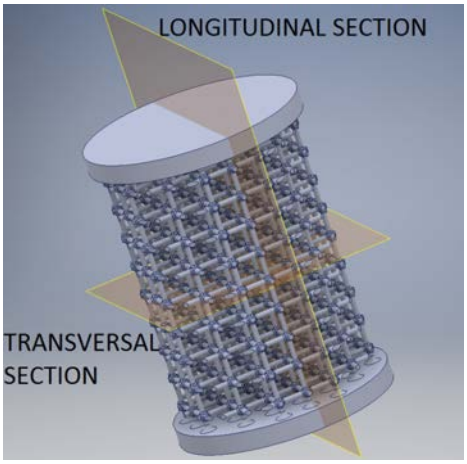

Figure 6. Definition of transversal and longitudinal sections of each cellular specimen.

Micro-hardness measurement

Microhardness profiles are measured to characterize the material's work hardening. A diamond Vickers indenter is used applying a maximum force of 1 N. The load is applied at a constant 0.1 N/s

rate with a dwell time of 10 s. Three measurements are performed at each depth and averaged to account for material's heterogeneity and measurement errors.

Quasi-static testing

An Instron 4500 testing machine was used for both compressive and tensile quasi-static test equipped with a 10 kN load cell (nonlinearity ± 0.1% of R.O.) and an axial extensometer (10 mm gauge length, nonlinearity ± 0.15% of R.O.). The crosshead speed was 0.5 mm/min.
The elastic modulus was measured by calculating the slope of loading-unloading cycles according to ISO 13314. This is necessary because both in compression and tension the slope of the first portion (the elastic part) of the stress-strain curve is lower than that of the successive unloading-loading curves due to local plastic effects (Ashby, 2000). The unloading-loading cycle was done between the 20% and the 70% of the compressive yield strength measured on identical specimens.
The yield strength both in tension and compression was determined as the 0.2% offset yield stress.
For each structure, three samples were tested under quasi-static conditions: one in tension, one in compression and one to calculate the elastic modulus (unloading-loading curve).

Fatigue testing

Axial fatigue tests were carried out in laboratory environment using a RUMUL Mikrotron 20 kN resonant testing machine equipped with a 1 kN load cell operating at a nominal frequency of 120 Hz under load control. The specimens were subjected to constant amplitude fully reversed fatigue cycles (zero mean stress, $R = -1$). To the author's best knowledge, until now additively manufactured Ti6Al4V cellular specimens have only been tested by compression-compression fatigue tests. This is normally justified by the fact that human bones are loaded prevalently in compression (Duda, 1997; Taylor, 1996). On the other hand, the authors wish to add to the body of knowledge regarding the mechanical behavior of biomedical cellular structures a worst-case scenario in which the flexural load acting on the implant is significant. Completely reversed fatigue is the standard test for fatigue and thus more material data is available and it is easier to interpret the results with models from the literature, in particular regarding the analysis of defects according to Murakami's approach (Beretta, 1998; Murakami, 2002), which is matter for future work. Also, this research is the natural prosecution of the work of Benedetti et al. (Benedetti, 2017), where bulk SLM samples have been tested under fully reversed fatigue. Some of the structures studied in this research are stretching dominated while others are bending dominated (Deshpande, 2001), thus the

cell walls are loaded differently. More specifically, in the case of compression-compression fatigue the stretching dominated structures work exclusively in compression while parts of the bending dominated structures still undergo tensile stresses. Thus, the two types would show a remarkably different behavior, to the advantage of the stretching dominated ones. In the case of completely reversed fatigue, the loading scenario is more equilibrated, as in both cases the struts are subjected to alternate normal stresses.

ha eliminato: stress

The high cycle fatigue resistance of the different structures has been estimated according to a method developed by Maxwell et al. (Maxwell, 1999) for Ti alloys that considerably reduces the testing time and the amount of expensive experimental material with respect to standard methods. This method consists in a step loading procedure that starts from a load below the one expected to cause failure at a chosen number N of cycles, viz. 10^6 in the present work. If the specimen survives, the load is increased by a small amount (5%) and the procedure is repeated in blocks of N cycles on the same specimen until failure. This is conventionally set as the condition in which the sample stiffness decreases by 10% with respect to the initial value. The fatigue limit for N cycles can be calculated by the following interpolating formula:

$$\sigma_{N-H} = \sigma_{pr} + \frac{N_f}{N}\left(\sigma_f - \sigma_{pr}\right) \tag{6}$$

where σ_{N-H} is the estimated fatigue limit at N cycles, σ_{pr} is the stress level reached at the loading block prior the last one (at which failure occurred), N_f is the number of cycles in the last block that produced failure and σ_f is the stress level at the last loading block. Thus, if the specimen fails at the first loading block this approach fails. A sample of three specimens was tested for each structure, for a total of 18 specimens (those failed prematurely were replaced to have an acceptable statistic).

The fatigue test was interrupted when the resonant frequency of the specimen decreased of 1 Hz with respect to the beginning of the test. This avoided the complete failure of the specimen and allowed to identify the first cell walls to fail by heat tinting. After the fatigue test the specimen was put in tension and put in a furnace, so that only the cell walls failed by fatigue were oxidized.

The fracture surfaces and the external sample surfaces are investigated under a JEOL JSM-IT300LV Scanning electron microscope, pictures are taken in both secondary and back-scattered electron, the quantitative chemical analysis is performed by EDXS probe.

The fatigue notch factor K_f is a parameter that quantifies the actual sensitivity to notches of a material by comparing the fatigue resistance of notched and unnotched specimens. K_f is calculated as:

$$K_f = \frac{\text{fatigue resistance of bulk specimen}}{\text{fatigue resistance of the cellular specimen}} \quad (7)$$

The fatigue resistance of the cellular specimens was calculated by dividing the force applied to the cellular structure by its nominal cross section (i.e. the section measured as if the cellular material was a bulk material). The rationale behind the present definition of K_f is that the cellular structure is intrinsically affected by notch effects and that the baseline fatigue resistance of the material can be estimated from fatigue tests carried out on bulk smooth samples.

ha formattato: Evidenziato
ha formattato: Evidenziato
ha formattato: Pedice , Evidenziato
ha formattato: Evidenziato

Biological tests

MG-63 cell line (Homo sapiens bone osteosarcoma; ATCC® CRL-1427™) were routinely cultured in Eagle's Minimum Essential Medium (MEME; Sigma-Aldrich) supplemented with 10% fetal bovine serum (Sigma–Aldrich), 1% L-glutamine (Sigma-Aldrich) and 1% penicillin and streptomycin (Sigma–Aldrich).

Cellular specimens both with cubic and cylindrical symmetry were sterilized in autoclave before placing in a 24-well plate. MG-63 cells were seeded at 5 x 104 cells/sample in 1 ml of medium, and cultured at 37 °C in a humidified atmosphere with 5% CO_2 concentration. Standard titanium disks were subjected to the same protocol to have comparison samples. Cell growth is assessed using the MTT reduction assay (Benedetti, 2017). This assay is based on the reduction operated by viable cells via specific mitochondrial enzymes of the MTT dye (3-(4,5-dimethylthiazol-2-yl)-2,5-diphenyltetrazolium bromide, Sigma-Aldrich) to insoluble formazan salts. Briefly, the cell-seeded metallic specimens were removed at fixed time from the original wells and-placed in fresh wells containing 0.5 ml of culture medium and 0.5 ml of a 0.4 mg/ml MTT solution in DPBS (Sigma-Aldrich). After 2 h of incubation, 1 ml of MTT solvent (i.e. 10% SDS in 0.01 N HCl) is added to each sample to dissolve the dark blue crystals and cells were cultured for 2 more hours at 37 °C and 5% CO2. Finally, the absorbance at 575 nm is measured using the Jasco V-550 UV–vis spectrophotometer.

The percentage of cell growth is calculated as follows:

$$cell\ growth\ (\%) = \frac{A_s - A_0}{A_c - A_0} \times 100 \quad (8)$$

where A_s is the absorbance value of the sample, A_c is the absorbance of cells grown on titanium disks (control) and A_0 is the blank value (no cells). All absorbance values are normalized to the total sample surface area.

2.4 Numerical modeling

FE models of the specimens were built by importing the CAD models in ANSYS® and meshing them with 10 node tetrahedral structural elements (SOLID187). Simulations were carried out to calculate the theoretical elastic modulus and the maximum stress from which the notch stress concentration factor was calculated, thus only the static standard solver was employed. The properties of bulk Ti6Al4V were used, with Young's modulus equal to 110000 MPa and Poisson's ratio equal to 0.3.

The expected mechanical properties of the structures were calculated from unit cells by applying the periodic boundary conditions as described in (Dallago, 2017). A convergence study was carried out for each solid model of the unit cell until the variation of the stress concentration factor was below 1%.

3. RESULTS AND DISCUSSION

3.1 Morphological characterization

The surface of the as-built specimen is covered with loosely attached unmelt particles (as can be seen in Figure 7a) that considerably increase the surface roughness. The HIPed specimens have a smoother surface (Figure 7b) thanks to the sand blasting treatment. On the other hand, the notches and the irregularities of the geometry (thickness and alignment of the cell walls) stay unchanged

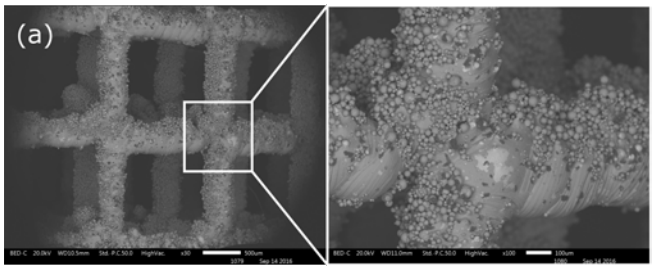

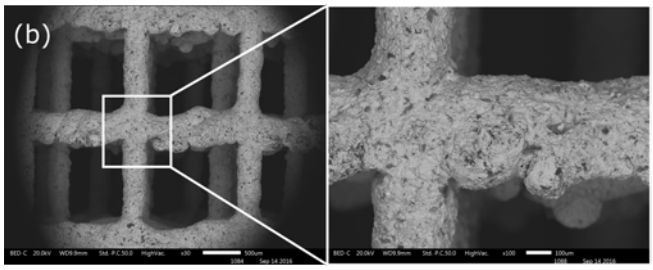

Figure 7. Surface appearance of the SLM Ti6Al4V specimens before (a) and after (b) HIP.

Longitudinal and transversal sections were cut from two specimens for each structure (one as-built and one HIPed) to carry out an in-depth analysis of the dimensional quality of the printed specimens. Thus, a total of 12 specimens were analyzed. As an example, in Figure 8 two transversal sections of a CUB S structure are shown, one before and one after the HIPing treatment. It is immediate to notice the decrease in porosity (pores are virtually absent in the HIPed specimen. On the other hand, it becomes clear that the fillet radii are highly irregular and do not resemble the CAD model. These observations are valid also for the other specimens, but pictures are not shown because of the limited space.

The actual geometrical parameters of the cellular structures were quantitatively analyzed to compare them with the CAD models. The cell wall thickness and the fillet radius were measured both on the transversal and longitudinal sections for each type of structure. This was done with a MATLAB routine that uses the standard image analysis functions embedded in the software. After binarizing the micrograph, the contours of the unit cells were extracted and by appropriately selecting the data points the fillet radii and the cell wall thicknesses were calculated. The fillet radius was estimated by trying to find the circle that fits the best the curvature of the cell wall junction, as shown in Figure 8. A statistic of the measured values was carried out and the mean values and the standard deviations were calculated.

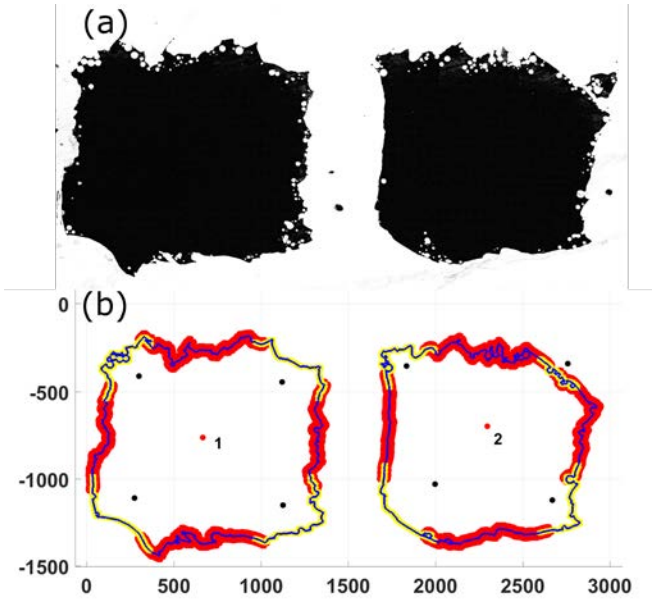

Figure 8. Detail of the procedure to estimate the fillet radius and the cell wall thickness from metallographic sections. This figure is purely demonstrative, the measurements are carried out on bigger images to have an appropriate statistic. (a) Micrograph to be analyzed (as built specimen, note the presence of pores); (b) MATLAB output: the yellow part of the contour are the data used to estimate the fillet radius, the red part of the contour are the data used to estimate the thickness of the horizontal and vertical cell walls, the red dot is the barycenter of the cell.

The plot of Figure 9 shows the fillet radius measured on the sections of the specimen with the respective standard deviation. The data points identified in the legend as “CAD” are the nominal values from the CAD files input to the printer (these point obviously do not have a standard deviation). The values of the fillet radius were difficult to measure since they were very badly reproduced by the printer and because of the very simple approach adopted. Observing the data, no correlation between the nominal values and the measured values can be found.

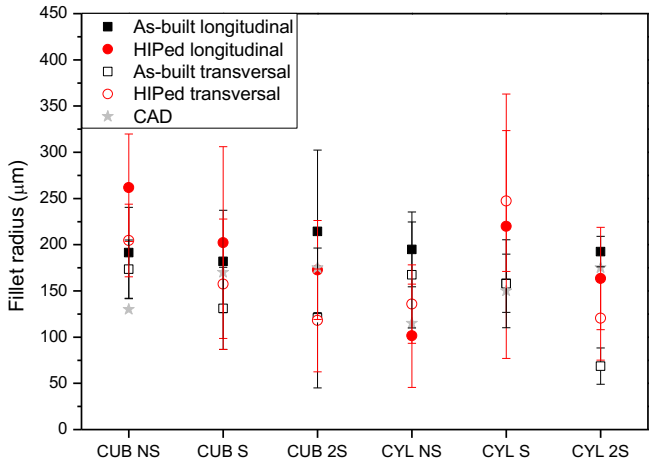

Figure 9. Mean value and standard deviation of the fillet radius calculated from the metallographic sections. The values are shown for the transversal (T) and longitudinal (L) sections with respect to the specimen axis.

The results of the metrological analysis on the strut diameter are shown in the plot of Figure 10. The measured cell wall diameters are reasonably close to the respective nominal values.

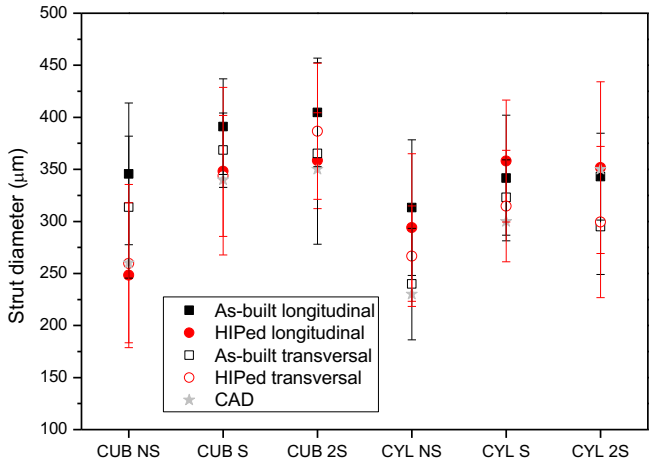

Figure 10. Mean value and standard deviation of the strut diameter calculated from the metallographic sections. The values are shown for the transversal (T) and longitudinal (L) sections with respect to the specimen axis.

3.2 Porosity analysis

In Figure 11 an example is shown of how the pores were counted and their area measured with ImageJ.

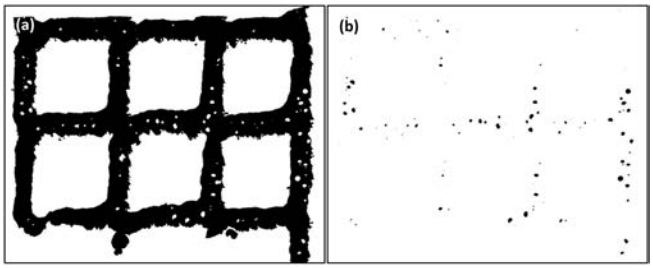

Figure 11. Metallographic section of an as built CUB-NS specimen (a) and its pores (b).

Porosity is strongly reduced by the HIP treatment (Figure 12 and Figure 13). It is possible to note how HIPing is particularly effective in reducing the size of the biggest pores. The cylindrical specimens are richer in pores than the cubic ones, this is most likely because the former ones are characterized by a more intricate geometry that is likely more complex to produce. It is also interesting to observe that both porosity and the size of the maximum pore tend to decrease with increasing staggering (NS → S → 2S). The authors believe that this can be explained with the fact that the cell wall thickness increases with staggering and thus a higher quality is obtained. This is also confirmed by Figure 10: the cell wall thickness measured on the staggered structures is closer to the nominal value.

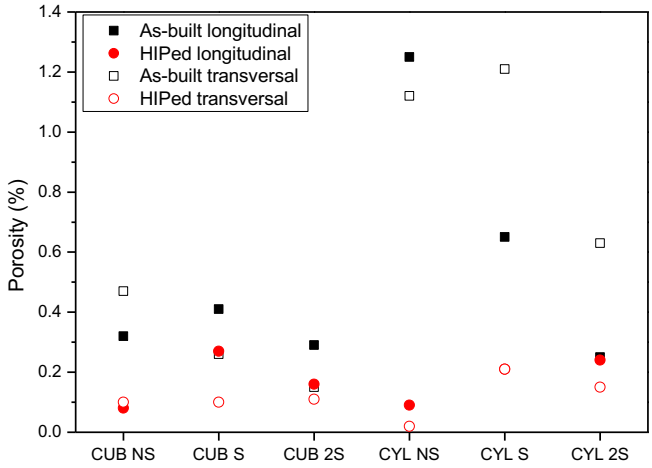

Figure 12. Porosity (%) calculated on the transversal (T) and longitudinal (L) sections with respect to the specimen axis.

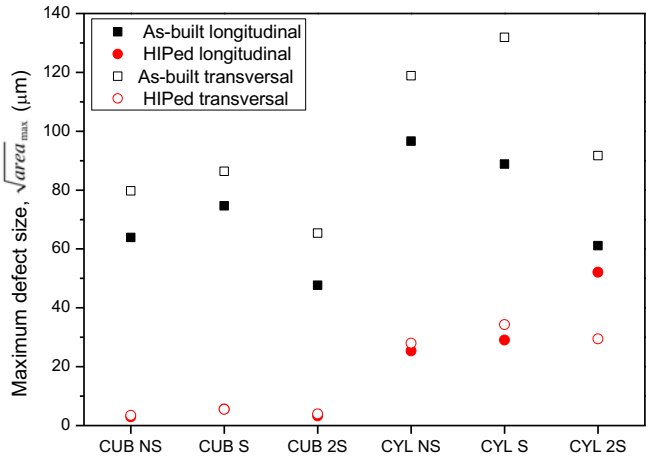

Figure 13. Maximum defect size expressed as $\sqrt{area}_{max}$. The pore sizes are shown for transversal (T) and longitudinal (L) sections with respect to the loading direction (specimen axis).

3.3 Microstructure

The as-built microstructure (Figure 14) is characterized by fine acicular martensite (α' phase). In the transversal section, some bigger plates are visible, which are most likely α phase. The effect of the HIP treatment on the microstructure is clearly shown in Figure 15. The microstructure is remarkably coarser, characterized by α lamellae in a β matrix (α+β structure). The micrographs shown are taken from the regular cylindrical structures (CYL-R), but these considerations apply to all the structures.

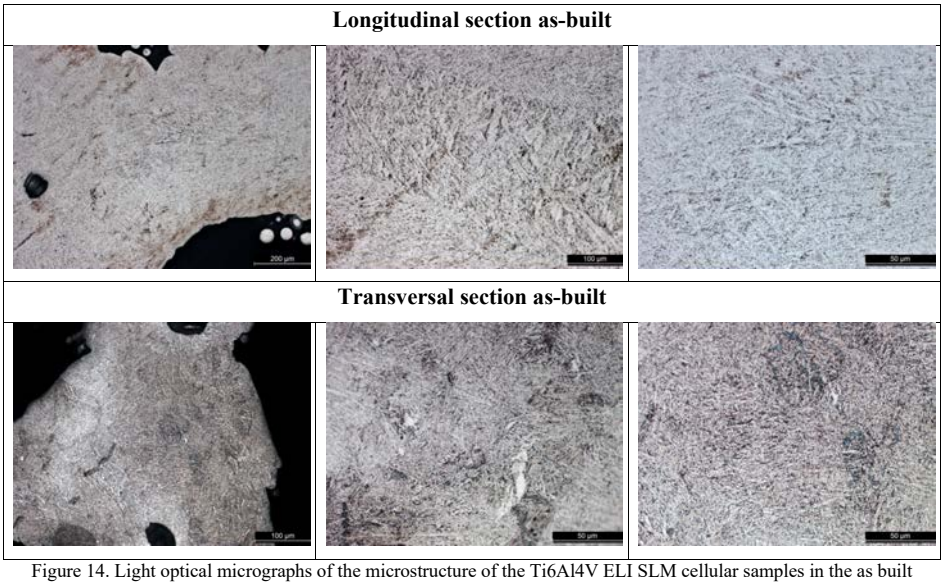

Figure 14. Light optical micrographs of the microstructure of the Ti6Al4V ELI SLM cellular samples in the as built condition.

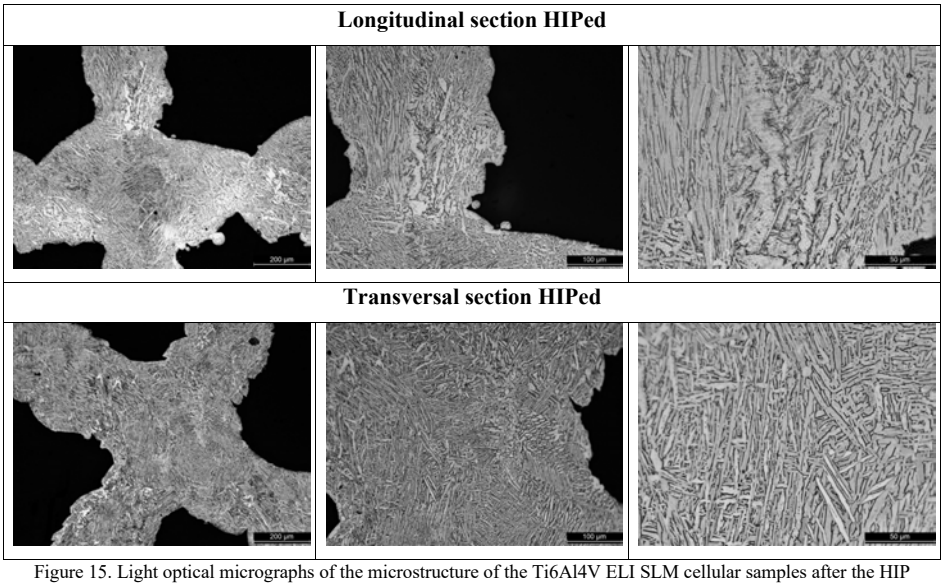

Figure 15. Light optical micrographs of the microstructure of the Ti6Al4V ELI SLM cellular samples after the HIP treatment.

3.4 Micro-hardness

The presence of a harder martensitic microstructure in the as-sintered samples is confirmed also by the indentation tests (Figure 16). Bulk samples of 3D printed (SLM) Ti6Al4V (both as-sintered and HIPed) have also been tested for micro-hardness (Benedetti, 2017). It is interesting to observe that the results of the as-sintered samples for both the cellular and the bulk (≈380 HV) ones are rather close, while those for the HIPed cellular samples compare only with the values of hardness close to the surface of the bulk samples (≈380 HV). This is because the deformed zones in the cellular samples extend well inside the struts because they are very thin.

The micro-hardness values do not show any clear dependence on the morphology of the structure, as was expected.

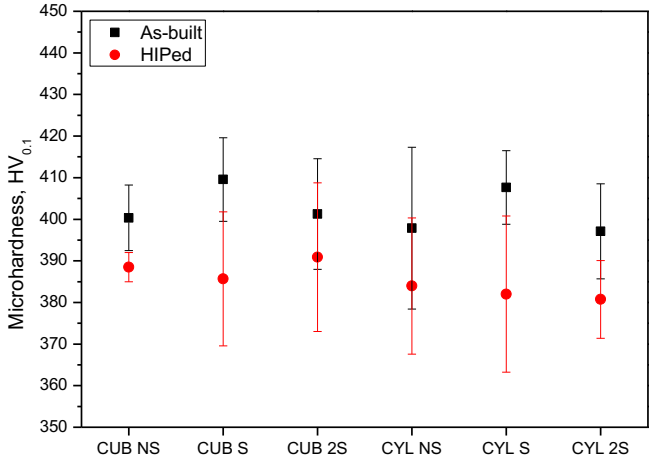

Figure 16. Results of the micro-hardness tests for each structure type in the as-built and the HIPed cases.

3.5 Static mechanical tests

The elastic moduli measured from the loading-unloading quasi-static are compared with those predicted by the finite element analyses based on the ideal geometry (Figure 17) and the measured values compare well with the theoretical ones.

Commentato [MB2]: Ti chiederei uno sforzo per commentare in modo più organico i risultati di questi test, anticipando qualitativamente quanto trovato da Benatti. Ti passo anche il grafico con il valore corretto del modulo elastico della struttura NS Potresti dire che in generale l'obiettivo di raggiungere il target dei 3GPa è stato raggiunto, nonostante le variazioni dimensionali riscontrate nei paragrafi precedenti. Queste sembrano influenzare più le proprietà a fatica che la rigidezza. Questa osservazione andrebbe anche rimarcata tra le conclusioni

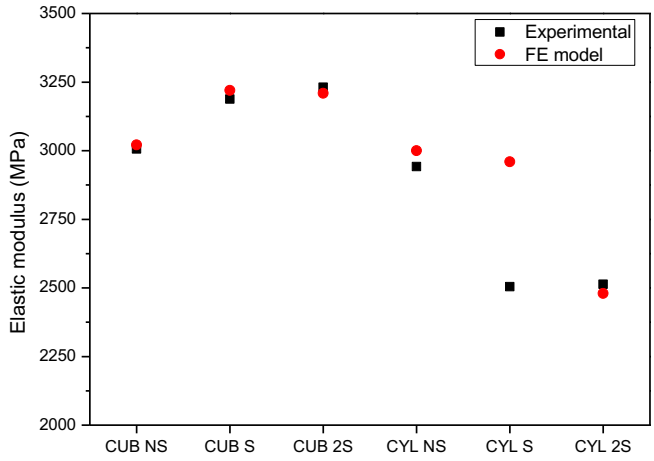

Figure 17. Comparison of the elastic modulus as calculated from the FE analyses based on the CAD model and the experimental values.

3.6 Fatigue tests

Figure 18 summarizes the results of the fatigue tests undertaken on the cellular samples. It can be noted that HIPing does not appear to have a clear effect on the fatigue resistance. The most reasonable explanation for this is that fatigue resistance is more controlled by the manufacturing quality in terms of the geometrical irregularities and especially the accuracy in reproducing the geometrical details at the junction between cell walls rather than by internal pores, which in turn are the main factor controlling the fatigue resistance of bulk materials fabricated via SLM. In fact, we have already discussed that the HIP treatment does not reduce the severity of notches that are invariably present at the wall junctions. In addition, the thermal treatment associated to HIPing reduces the material microhardness, negatively impacting on the fatigue resistance of SLM manufactured Ti-6Al-4V, as observed in (Benedetti, 2018).

On the other hand, the data also suggest that staggering has a positive effect on fatigue resistance and this effect is more marked for the cubic samples. The most likely explanation for this can be obtained by carefully reading Table 3 in which the SCFs calculated from the FE simulations are listed for each structure. The maximum stresses in the staggered cubic specimens decrease remarkably with staggering because the cell wall thickness and the fillet radius both increase. The same does not apply to the cylindrical structures because of the more complicated design that causes a non-uniform distribution of loads on the transversal section of the staggered structures.

ha formattato: Evidenziato
ha eliminato: (Figure 18).
ha eliminato: and not
ha eliminato: the
ha formattato: Evidenziato
ha formattato: Evidenziato
ha formattato: Evidenziato
ha eliminato:

Thus, some walls carry more load than others and the tensions are higher at the corresponding junctions despite the higher values of t_0 and R.

In compressive-compressive fatigue tests, structures with small or absent bending actions (as the cubic structure) show very high fatigue resistance (Yavari, 2015). Since our study is concerned with push-pull fatigue, all the structures are subjected to tensile stresses, included the cubic ones, and thus the fatigue strengths measured are not comparable with those reported in other works. We observed that the fatigue resistance is in fact higher for structures with prevalently bending actions, but this is because those structures have thicker struts (given that the nominal elastic modulus is the same for all structures) and thus lower stresses. As observed also by Zargarian et al. (Zargarian, 2016), the effect of the strut cross section size appears to have the strongest influence on the fatigue strength, compared to the relative density (and given the same base material).

The fatigue stress concentration factors K_f could be computed because the fatigue resistance at 10^6 cycles of SLM unnotched bulk Ti6Al4V specimens was measured, both in the heat treated and the HIPed conditions (Benedetti, 2017) and reported in Table 4. The fatigue notch factors are reported in Table 3. The fatigue notch factor K_f should be lower than or at most equal to K_t (Dowling, 2013), but in this case, it is not. This indicates that the actual K_t is much higher than that predicted based on the ideal geometry. This suggests that the irregularities introduced during the manufacturing process have a strong effect on the fatigue properties. It is worth to note that the notch factors are very high because of the way in which they are defined (see Eqs. 4 and 7).

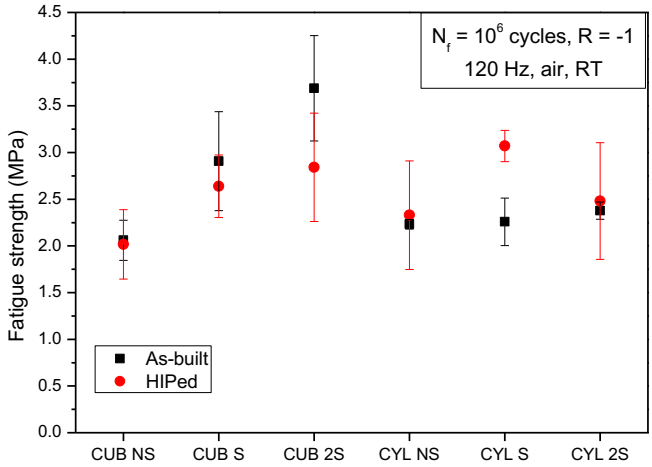

Figure 18. Fatigue resistance at 10^6 cycles for each structure type with error bars.

Table 3. Stress concentration factor and fatigue notch factors for each structure.

Structure	K_t	K_f as-built	K_f HIPed
CUB NS	62	115	188
CUB S	49	82	144
CUB 2S	37	65	133
CYL NS	58	107	163
CYL S	59	105	123
CYL 2S	68	100	153

Table 4. Fatigue resistance at 10^6 cycles for SLM bulk titanium specimens (Benedetti et al., 2017).

	As-built		HIPed	
	Mean	Std. dev.	Mean	Std. dev.
σ_{10^6} **bulk specimens [MPa]**	238	24	379	21

The front of fatigue-failed cell walls propagates from the exterior to the interior of the specimen and this is a characteristic common to all the specimens. In Figure 19 a fractured section of a CUB S specimen after heat tinting is shown as an example. In our view, this is most likely due to the specimen not being perfectly aligned with the machine grips and the consequent bending load.

ha eliminato: fatigue failed

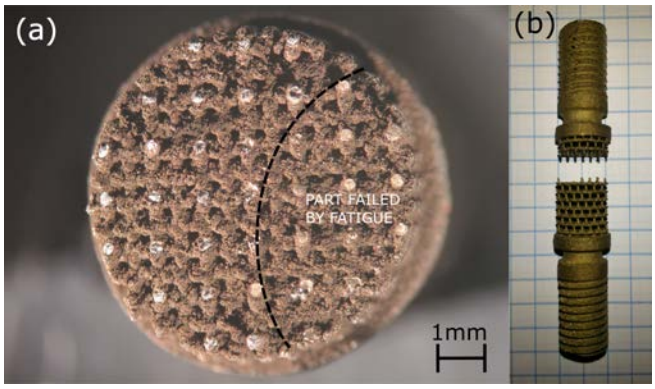

Figure 19. (a) Fractured section of a fatigue testes specimen (as built CUB S). The cell walls failed by fatigue (in the area indicated as “part failed by fatigue”) are golden because of the heat tinting. (b) Fractured specimen after a fatigue test. The fracture is away from the bulk/cellular interface.

The fractured sections of the fatigue specimens were observed with the SEM to have a better understanding of the damage process and the following observations could be made, which apply to all the structures:

- the fatigue crack front propagates across the specimen section as one cell wall breaks after the other to the other due to the cyclic loading until the stiffness of the structure decreases enough to stop the test.
- The fracture in almost every specimen propagates in a single plane, i.e. it rarely moves away from the transversal plane. The specimens generally break away from the bulk part, due to the thicker cell walls of the first plane of unit cells. This behavior is different from that observed in compressive-compressive fatigue tests, where the failed struts are located along a plane inclined of 45° at the load direction (van Hooreweder, 2017).
- The cell walls always break at the cell wall junctions where, according to the FE analyses, the stresses should be higher. The critical role of the junctions as stress raisers is observed also in compression-compression fatigue tests (Zhao, Li, Hou, Hao, Yang R., Misra, 2016; de Krijger, 2017; van Hooreweder, 2017), although in that kind of fatigue test the unit cell geometry has a critical effect because it determines whether bending (and thus tensile stresses) or axial actions (and thus only compressive stresses) prevail. In push-pull tests, on the other hand, the geometry of the unit cell does not appear so crucial compared to the stress concentration factor, given that tensile stresses cannot be avoided.
- The fatigue crack in the cell wall section typically originates from surface irregularities and not from internal pores, as shown in Figure 20.

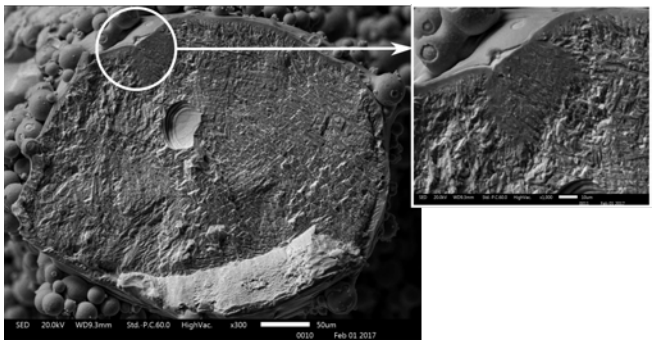

Figure 20. Fractured section of a cell wall of an as-built CYL-S specimen after termination of the fatigue test. Note that the fatigue crack nucleated on the surface (detail) and not at the pore.

3.7 Biological tests

To check the propensity of bone cells to grow and colonize the titanium cellular specimen, a proliferation test was performed. Bone osteosarcoma cells (i.e. MG-63 cell line) were seeded on titanium samples and let in incubation for a period of time spanning from 24 to 90 h. Cell growth at the desired time was calculated for samples with different symmetry by comparison with titanium disks, treated in the same experimental conditions and arbitrary selected as controls. Three samples were tested to represent both the symmetry (cylindrical or cubic, i.e. CYL NS and CUB NS respectively) and the structure characteristics (non-staggered or staggered, i.e. NS or 2S respectively) of the cellular specimen. The three samples showed similar behavior in terms of cell growth when incubated for short time (Fig. 21, up to 66 h), while after 90 h the CUB-NS sample seemed more suitable for cell growth. The growth on this sample was indeed slightly better even at shorter incubation times, but after 90 h the difference with the other tested samples was clearly visible and significant. As a general trend, the cylindrical symmetry seems the most unfavorable for cell growth with respect to the cubic symmetry. Considering instead the structure characteristics, the cell growth decreased passing from a non-staggered structure (i.e. CUB NS) to a double staggered structure with the same symmetry (i.e. CUB 2S). Since the unit cell pore size for the CUB NS and the CYL NS specimens is the same, these results are puzzling. On the other hand, the CYL NS structure has bigger voids than the CUB NS to the cylindric symmetry. Very likely this is detrimental to cell growth, but further studies are necessary in order to verify this statement.

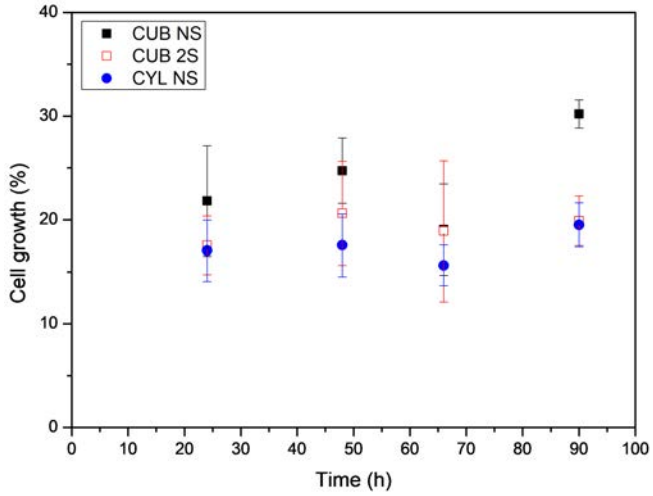

Fig. 21: MG-63 cell growth on the cellular specimen with different symmetry at different times of incubation. Percentages are calculated with respect to cell grown on standard titanium disks. Mean of 4-8 independent measures and standard errors are shown.

The combined biological and mechanical (fatigue) characterization done so far stimulates some comments on which structure and which treatment gives the best combination of properties. The cylindrical structures gave the worst performance both from the fatigue and the biological point of view and thus in general the cubic ones appear to be a better choice for load-bearing biomedical implants. The effect of staggering appears to improve fatigue resistance to the detriment of cell growth. Given this observation, the ideal implant might be one that shows a transition of unit cell morphology form the surface (regular cubic, to favor osseointegration) to the interior (staggered cubic, to improve the fatigue resistance of the whole component).

ha eliminato: together allow to make

ha eliminato:

4. CONCLUSIONS

The present paper presents the results of the mechanical, dimensional and biological characterization of different regular cubic open-cell cellular structures produced by SLM of Ti6Al4V alloy. The main objective of this research was to determine which one has the best fatigue resistance. These structures are intended to be employed in the production of fully porous orthopedic implants. Six different configurations of the cubic cell were chosen: in three of them the cubes are simply shifted to fill the 3D space, while in the other three the cubic cells are skewed to obtain structures with cylindrical symmetry. Some of the structures studied in this research are stretching dominated while others are bending dominated (Deshpande, 2001), thus the cell walls are loaded differently. Each cellular specimen was provided with threaded heads to carry out fully reversed fatigue tests and both compressive and tensile quasi-static tests. An extensive dimensional analysis was carried out on specimens for each type to assess the quality of the manufacturing process and the discrepancy between the actual measured cell parameters and the nominal CAD values. The effect of the manufacturing defects (porosity, surface roughness and geometrical inaccuracies) on the mechanical properties is investigated and discussed. The fracture surfaces of the cell walls of the specimens broken by fatigue were observed by SEM and the fracture behavior of each structure is discussed based on these observations. Half of the specimens was subjected to HIP and the effect of this treatment on porosity and the mechanical properties was investigated.
The following conclusions could be drawn:

ha eliminato: a

ha eliminato: cylindric

- The HIPing treatment considerably reduces internal porosity, but it does not have a clear effect on fatigue resistance because fatigue resistance is not affected as much by internal porosity as by surface defects, especially sharp notches.
- Cellular structures designed with thicker cell walls (the staggered structures) appear to be less affected by internal porosity.
- The values of the elastic modulus compare well with those predicted by the finite element analyses based on the ideal geometry. This indicates that the elastic modulus is not sensitive to the irregularities introduced during the manufacturing process.
- The effect of shifting the unit cells (staggering) to introduce bending actions in the cell walls is positive on the fatigue resistance because to keep the same elastic modulus as for the regular structures thicker cell walls and fillet radii are necessary and thus the stress concentrations are lower.
- The fact that K_f is much higher than the K_t predicted based on the ideal geometry suggests that the irregularities introduced during the manufacturing process have a strong effect on the fatigue properties. In general, the ideal geometry causes the overestimation of the fatigue properties because it does not obviously consider the fact that the additive manufacturing process is not always able to exactly replicate the geometry.
- The results of the cell proliferation tests indicate that the cubic structures are more suitable for bone cell growth, with a weaker performance shown by the staggered structure compared to the regular one. The ideal implant might be one that shows a transition of unit cell morphology form the surface (regular cubic, to favor osseointegration) to the interior (staggered cubic, to improve the fatigue resistance of the whole component).
- The SLM technique has been pushed to its limits in printing the fine details of the designed specimens. Probably the current technology is unable to accurately reproduce the design at this level and thus to achieve the desired details (the fillet radius) it is advisable to use thicker cell walls.

Future work

The results presented here are promising and allow for a broad spectrum of future developments. The authors plan to study more accurately the morphology and the porosity of the printed specimens via CT scans. This permits also to import the structures into a FE software to estimate the real stress concentration factors.

ha eliminato: allows

Acknowledgments

The authors wish to thank Dr. M. Cazzolli and Mr. V. Luchin for their contributions to the design of the specimens. This work was financially supported by the University of Trento, within the strategic research project 2014 (under grant P.STR.14 3D) entitled “3D printed metallic foams for biomedical applications: understanding and improving their mechanical behavior”.

REFERENCES

Ahmadi S., M., Yavari S. A., Wauthle R., Pouran B., Schrooten J., Weinans H., Zadpoor A. A., Additively manufactured open-cell porous biomaterials made from six different space-filling unit cells: the mechanical and morphological properties, Materials 8 (2015), pp. 1871-1896

Ahn Y.-K., Kim H.-G., Park H.-K., Kim G.-H., Jung K.-H., Lee C.-W., Kim W.-Y., Lim S.-H., Lee B.-S., Mechanical and microstructural characteristics of commercial purity titanium implants fabricated by electron-beam additive manufacturing, Materials Letters 187 (2017), pp. 64-67

Albrektsson T., Johansson C., Osteoinduction, osteoconduction and osseointegration, Eur Spine J 10 (2001), pp. S96–S101

Arabnejad S., Burnett Johnston R., Pura J. A., Singh B., Tanzer M., Pasini D., High-strength porous biomaterials for bone replacement: A strategy to assess the interplay between cell morphology, mechanical properties, bone ingrowth and manufacturing constraints, Acta Biomaterialia 30 (2016), pp. 345–356

Ashby M.F., Evans A.G., Fleck N.A., Gibson L.J., Hutchinson J.W., Wadley H.N.G., Metal Foams: A Design Guide, Butterworth-Heinemann (2000)

Benedetti M., Torresani E., Leoni M., Fontanari V., Bandini M., Pederzolli C., Potrich C., The effect of post-sintering treatments on the fatigue and biological behavior of Ti-6Al-4V ELI parts made by selective laser melting, J. Mech. Behav. Biomed. Mater. 71 (2017), pp. 295–306

Benedetti M., Fontanari V., Bandini M., Zanini F., Carmignato S., Low- and high-cycle fatigue resistance of Ti-6Al-4V ELI additively manufactured via selective laser melting: Mean stress and defect sensitivity, International Journal of Fatigue 107 (2018), pp. 96-109

ha formattato: Evidenziato

Beretta S., Murakami Y., Statistical analysis of defects for fatigue strength prediction and quality control of materials, Fatigue & Fracture of Engineering Materials & Structures 21 (1998), pp. 1049-1065

Campoli G., Borleffs M.S., Yavari S.A., Wauthle R., Weinans H., Zadpoor A.A., Mechanical properties of open-cell metallic biomaterials manufactured using additive manufacturing, Materials and Design 49 (2013), pp. 957-965

Dabrowski B., Swieszkowski W., Godlinski D., Kurzydlowski K. J., Highly porous titanium scaffolds for orthopaedic applications, Journal of Biomedical Materials Research B: Applied Biomaterials 95B (2010), Issue 1

Dallago M., Benedetti M., Luchin V., Fontanari V., Orthotropic elastic constants of 2D cellular structures with variously arranged square cells: The effect of filleted wall junctions, International Journal of Mechanical Sciences 122 (2017), pp. 63-78

de Krijger J., Rans C., Van Hooreweder B., Lietaert K., Pouran B., Zadpoor A. A., Effects of applied stress ratio on the fatigue behavior of additively manufactured porous biomaterials under compressive loading, Journal of the Mechanical Behavior of Biomedical Materials 70 (2017), pp. 7-16

Deshpande V. S., Ashby M. F., Fleck N. A., Foam Topology Bending versus Stretching Dominated Architectures, Acta mater. 49 (2001), pp. 1035-1040

Duda G. N., Schneider E., Chao E. Y., Internal forces and moments in the femur during walking, J Biomech. 30 (1997), Issue 9, pp. 933-41.

Dowling N. E., Mechanical Behavior of Materials, Fourth Ed. (2013), Pearson

Gong H., Rafi K., Gu H., Ram G. D. J., Starr T., Sticker B., Influence of defects on mechanical properties of Ti6Al4V components produced by selective laser melting and electron beam melting, Materials and Design 86 (2015), pp. 545-554

Hrabe N. W., Heinl P., Flinn B., Körner C., Bordia R. K., Compression-compression fatigue of selective electron beam melted cellular titanium (Ti-6Al-4V), J Biomed Mater Res Part B (2011) 99B, pp. 313–320

Khanoki S. A., Pasini D., Fatigue design of a mechanically biocompatible lattice for a proof-of-concept femoral stem, Journal of the Mechanical Behavior of Biomedical Materials 22 (2013), pp. 65-83

ha eliminato: ¶

Leuders S., Thoene M., Riemer A., Niendorf T., Troester T., Richard H. A., Maier H. J., On the mechanical behavior of titanium alloy Ti6Al4V manufactured by selective laser melting: Fatigue resistance and crack growth performance, International Journal of Fatigue 48 (2013), pp. 300-307

Li S. J., Murr L. E., Cheng X. Y., Zhang Z. B., Hao Y.L., Yang R., Medina F., Wicker R. B., Compression fatigue behavior of Ti–6Al–4V mesh arrays fabricated by electron beam melting, Acta Materialia 60 (2012), pp. 793–802

Li S. J., Xu Q. S., Wang Z., Hou W. T., Hao Y. L., Yang R., Murr, L. E., Influence of cell shape on mechanical properties of Ti6Al4V meshes fabricated by electron beam melting, Acta Biomaterialia 10 (2014), pp. 4537-4547

Long M., Rack H. J., Titanium alloys in total joint replacement – a materials science perspective, Biomaterials 19 (1998), pp. 1621-1639

Luxner M. H., Stampfl J., Pettermann H. E., Numerical simulations of 3D open cell structures – influence of structural irregularities on elasto-plasticity and deformation localization, International Journal of Solids and Structures 44 (2007), pp. 2990-3003

Luxner M. H., Stampfl J., Pettermann H. E., Nonlinear simulations on the interaction of disorder and defects in open cell structures, Computational Materials Science 47 (2009), pp. 418-428

Luxner M. H., Woesz A., Stampfl J., Fratzl P., Pettermann H. E., A finite element study on the effects of disorder in cellular structures, Acta Biomaterialia 5 (2009), pp. 381-390

Maxwell D. C., Nicholas T., A rapid method for generation of a Haigh diagram for high cycle fatigue, Fatigue and Fracture Mechanics: Twenty-Ninth Volume, ASTM STP 1332, Panontin T. L. and Sheppard S. D., Eds., American Society for Testing Materials, West Conshohocken (1999), PA

Murakami Y., Metal Fatigue: Effects of Small Defects and Nonmetallic Inclusions, Elsevier, 2002

Murr L. E., Gaytan S. M., Medina F., Martinez E., Martinez J. L., Hernandez D. H., Machado B. I., Ramirez D. A., Wicker R. B., Characterization of Ti6Al4V open cellular foams fabricated by additive manufacturing using electron beam melting, Materials Science and Engineering A 527 (2010), pp. 1861-1868

Murr L. E., Gaytan S. M., Ramirez D. A., Martinez E., Hernandez J., Amato K. N., Shindo P. W., Medina F. R., Wicker R. B., Metal Fabrication by Additive Manufacturing Using Laser and Electron Beam Melting Technologies, J. Mater. Sci. Technol. 28 (2012), Issue 1, pp. 1-14

Niinomi M., Mechanical biocompatibilities of titanium alloys for biomedical applications, Journal of the Mechanical Behavior of Biomedical Materials 1 (2008), pp. 30-42

Otsuki B., Takemoto M., Fujibayashi S., Neo M., Kokubo T., Nakamura T., Pore throat size and connectivity determine bone and tissue ingrowth into porous implants: Three-dimensional micro-CT based structural analyses of porous bioactive titanium implants, Biomaterials 27 (2006), pp. 5892–5900

Qiu C., Adkins N. J. E., Attallah M. M., Microstructure and tensile properties of selectively laser-melted and HIPed laser-melted Ti6Al4V, Materials Science & Engineering A 578 (2013), pp. 230-239

Rack H.J., Qazi J.I., Titanium alloys for biomedical applications, Materials Science and Engineering C 26 (2006), pp. 1269 – 1277

Ryan G., Pandit,A., Apatsidis D. P., Fabrication methods of porous metals for use in Orthopaedic applications, Biomaterials 27 (2006), pp. 2651-2670

Singh R., Lee, P. D., Dashwood, R. J., Lindley, T. C., Titanium foams for biomedical applications: a review, Materials Technology 25 (2010), No. ¾

Tammas-Williams S., Withers P. J., Todd I., Prangnell P. B., The effectiveness of hot isostatic pressing for closing porosity in titanium parts manufactured by selective electron beam melting, Metallurgical and materials Transactions A 47A (2016)

Tan X. P., Tan Y. J., Chow, C. S. L. Tor, S. B. Yeong, W. Y., Metallic powder-bed based 3D printing of cellular scaffolds for orthopaedic implants: A state-of-the-art review on manufacturing, topological design, mechanical properties and biocompatibility, Materials Science and Engineering C 76 (2017), pp. 1328-1343

Taniguchi N., Fujibayashi S., Takemoto M., Saski K., Otsuki B., Nakamura T., Matsushita T., Kokubo T., Matsuda S., Effect of pore size on bone ingrowth into porous titanium implants fabricated by additive manufacturing: An in vivo experiment, Materials Science and Engineering C (2016), pp. 690-701

Taylor M. E., Tanner K. E., Freeman M. A., Yettram A. L., Stress and strain distribution within the intact femur: compression or bending?, Med Eng Phys. 18 (1996), Issue 2, pp. 122-131

Van Hooreweder B., Apers Y., Lietaert K., Kruth J.-P., Improving the fatigue performance of porous metallic biomaterials produced by Selective Laser Melting, Acta Biomaterialia 47 (2017), pp. 193-202

Vrancken B., Thijs L., Kruth J.-P., Van Humbeeck J., Heat treatment of Ti6Al4V produced by Selective Laser Melting: Microstructure and mechanical properties, Journal of Alloys and Compounds 541 (2012), pp. 177–185

Wauthle R., Vrancken B., Beynaerts B., Jorissen K., Schrooten J., Kruth J.-P., Van Humbeek, J., Effects of build orientation and heat treatment on the microstructure and mechanical properties of selective laser melted Ti6Al4V lattice structures, Additive manufacturing 5 (2015), pp. 77-84

Wu S., Liu X., Yeung K. W. K., Liu C., Yang X., Biomimetic porous scaffolds for bone tissue engineering, Materials Science and Engineering R 80 (2014), pp. 1-36

Yavari S. A., Wauthle R., van der Stok J., Riemslag A.C., Janssen M., Mulier M., Kruth J. P., Amin Schrooten J., Weinans H., Zadpoor A. A., Fatigue behavior of porous biomaterials manufactured using selective laser melting, Materials Science and Engineering C 33 (2013), pp. 4849–4858

Yavari S. A., Ahmadi S. M., Wauthle R., Pouran B., Schrooten J., Weinans H., Zadpoor A. A., Relationship between unit cell type and porosity and the fatigue behavior of selective laser melted meta-biomaterials, Journal of the Mechanical Behavior of Biomedical Materials 43 (2015), pp. 91-100

Zargarian A., Esfahanian M., Kadkhodapour J., Ziaei-Rad S., Numerical simulation of the fatigue behavior of additive manufactured titanium porous lattice structures, Materials Science and Engineering C 60 (2016), pp. 339-347

Zhao S., Li S. J., Hou W.T., Hao Y.L., Yang R., Misra R. D. K., The influence of cell morphology on the compressive fatigue behavior of Ti-6Al-4V meshes fabricated by electron beam melting, Journal of the Mechanical Behavior of Biomedical Materials 59 (2016), pp. 251-264

Zhao S., Li S. J., Hou W. T., Hao Y. L., Yang R., Murr L. E., Microstructure and mechanical properties of open cellular Ti–6Al–4V prototypes fabricated by electron beam melting for biomedical applications, Materials Technology 31 (2016), Issue 2, pp. 98-107

Zhao X., Li S., Zhang M., Liu Y., Sercombe T. B., Wang S., Hao Y., Yang R., Murr L. E., Comparison of the microstructures and mechanical properties of Ti–6Al–4V fabricated by selective laser melting and electron beam melting, Materials and Design 95 (2016), pp. 21-31